Journal of Power Sources 195 (2010) 2851–2862

Contents lists available at ScienceDirect

Journal of Power Sources

journal homepage: www.elsevier.com/locate/jpowsour

Porous cathode optimization for lithium cells: Ionic and electronic conductivity, capacity, and selection of materials

Y.-H. Chen [a], C.-W. Wang [a], X. Zhang [a], A.M. Sastry [a,b,c,*]

[a] Department of Mechanical Engineering, University of Michigan, Ann Arbor, MI 48109-2125, USA
[b] Department of Biomedical Engineering, University of Michigan, Ann Arbor, MI 48109-2125, USA
[c] Department of Material Science and Engineering, University of Michigan, Ann Arbor, MI 48109-2125, USA

ARTICLE INFO

Article history:
Received 6 November 2009
Accepted 10 November 2009
Available online 13 November 2009

Keywords:
Li-ion battery
Battery design and optimization
Battery modeling
Electronic and ionic conductivity

ABSTRACT

Narrowing the gap between theoretical and actual capacity in key Li-based battery systems can be achieved through improvements in both electronic and ionic conductivities of materials, via addition of conductive species. Additives do, however, penalize both volumetric and gravimetric properties, and also limit liquid transport and high rate performance. In this work, we developed a technique to design and optimize cathode system based directly on the relationships among ionic and electronic conductivities and specific energy, for a range of commercially viable cathode electrochemistries and additives. Our results quantify trade-offs among ionic and electronic conductivity, and conductivity and specific energy. We also provide quantitative relationships for improved utilization and specific power, with higher specific energy. Finally, we provide quantitative guidance for the design of high energy density $Li(Ni_{1/3}Co_{1/3}Mn_{1/3})O_2$ cells using conductive additives, and also provide guidelines for the design of cathode systems, based directly on solid and liquid phase transport limitations. Future work will focus on higher rates of performance, and will be based on analyses here.

1. Introduction

A key culprit in limiting performance of Li-ion cells is inadequate conductivity, both electronic and ionic. Presently, the gap between theoretical and actual capacities at 1*C* rate in leading Li-based technologies are 32.3%, 31.9% and 38.1% in $LiFePO_4$, $Li(Ni_{0.8}Co_{0.15}Al_{0.05})O_2$ and $Li(Ni_{1/3}Co_{1/3}Mn_{1/3})O_2$, respectively [1–3]. The relationship between electronic and ionic conductivity is also problematic, absent mathematical optimization, because an increase in one generally penalizes the other. Porous electrodes, used in numerous industrial applications due to high achievable reaction rates, including Li batteries [4], must balance these needs.

Individually, various parameters have been examined for improving cell performance. Adjustments in form factor [5–7], cathode particle size [8–12], porosity and thickness of the cathode electrode and separator [13], electrolyte concentration [13], loading schema for conductive additives [14–18], and cathode particle arrangement [19] have all been shown to improve performance. Among these, improvements in transport properties, ionic and electronic conductivity, have been empirically shown to have the greatest effect. To date, however, no comprehensive numerical study has been reported which studies the optimization of these parameters via addition of conductive materials.

Continuum, porous electrode models [13,20–22], equivalent circuit models [23–25], atomistic [26,27], and molecular dynamics models [28,29], have been widely used to model cells. However, the variation of electrode material properties due to structural complexities has not, to date, been addressed. Thus, these scales of simulations do not directly inform engineering of cathode architecture designs via selection of additives. Few consider ion and electron transport [12,21], and none correlate conductivities to battery performance. Cathode design requires mesoscale simulations with various loading schema, but to date, there is little work in this area [19].

Optimization of battery design will undoubtedly replace sequential testing of various cathodic electrochemistries (i.e. those in Table 1 [1–3,30–33]). This is the preferred path in better matching theoretical and actual capacity, by selecting combinations of high power and energy density materials. In this study, a numerical, finite element model at the particle scale was applied to simulate porous effective ionic and electronic conductivities in cathodes with additives. Those effective properties were introduced to porous electrode model to simulate the battery performance. An

* Corresponding author at: University of Michigan, 2250 G.G. Brown Building, 2350 Hayward Street, Ann Arbor, MI 48109-2125, USA. Tel.: +1 734 764 3061; fax: +1 734 647 3170.
E-mail addresses: cyenhung@umich.edu (Y.-H. Chen), amsastry@umich.edu (A.M. Sastry).
URL: http://www-personal.engin.umich.edu/ amsastry (A.M. Sastry).

0378-7753/$ – see front matter © 2009 Published by Elsevier B.V.
doi:10.1016/j.jpowsour.2009.11.044

Table 1
Theoretical capacity and actual discharge capacity of different cathode materials.

Cathode material	General properties	Theoretical capacity ($mAh\,g^{-1}$)	Discharge capacity ($mAh\,g^{-1}$)	Utilization	Rate	Additives	Reference
$LiCoO_2$	Easy to prepare	274	180	0.66	*C*/10	Coated with Al_2O_3 7% CB	[30]
$LiNi_{1-x}Co_xO_2$	High capacity Low cost	274 $x=0.2$	176	0.64	*C*/10	10% CB	[31]
$LiMn_2O_4$	Low capacity	148	135	0.91	*C*/24	32% CB	[32]
	High rate		122	0.90	*C*/5		
	Low cost		120	0.81	1*C*	10% CB	[33]
$LiFePO_4$	High energy density	170	155	0.91	*C*/25	6% CB	[1]
	Low electronic conductivity Low cost		115	0.68	1*C*	6% graphite	
$Li(Ni_{0.8}Co_{0.15}Al_{0.05})O_2$	High specific energy High power	279	190	0.68	1*C*	3% CB	[2]
$Li(Ni_{1/3}Co_{1/3}Mn_{1/3})O_2$	High energy	278	185	0.67	*C*/10	40% teflonized acetylene black	[3]
	High capacity Good cycle performance		172	0.62	1*C*		

optimization approach, similar to Ref. [12], was applied to simplify numerical computation and to make analysis and optimization feasible. The current study focuses on numerical study for the cathode design for plug-in hybrid electrical vehicle (HEV) applications. Specific operating conditions will be selected and experimental comparison of battery performance will be neglected in the paper. Our objectives of this study were as follows:

(1) To demonstrate predictive methods of both ionic and electronic conductivity, and to validate predictions of electronic conductivity.
(2) To map relationship between the ionic and electronic conductivities with additives.
(3) To correlate conductivities to battery performance.
(4) To identify optimal schema for high energy $Li(Ni_{1/3}Co_{1/3}Mn_{1/3})O_2$ cells for plug-in HEV application.

2. Methods

From our previous research [18], we have successfully created the random particulate structure with cathode particles and additives via elastic collision model, and allowing the effective electronic conductivity can be predicted via the multi-phase finite model. In our previous findings, the porosity and the material types and shapes of conductive additives used, as well as connectivity, strongly influence effective electronic conductivity in a cathode system. The ionic conductivity can also be modeled by the same technique. To date, however, there have been no systematic studies published which identify the optimal amount of the conductive additives, considering ionic conductivity as well as quantitative models of morphology. Indeed, addition of excess conductive additives not only penalizes gravimetric properties, but also reduces ionic conductivity. In our current paper, we investigated both cathode (electronic) and electrolytic (ionic) conductivities based on our prediction technique [18], and the 1D/2D multi-physics finite model was used to simulate battery performance with predicted conductivities as inputs. After these simulations, optimization approach was used to further analyze and optimize combinations of materials.

Table 2 lists the material properties of electrodes and electrolyte [18,34–36] studied. In this research, $Li(Ni_{1/3}Co_{1/3}Mn_{1/3})O_2$ was selected as the active material with PVDF as binder. Graphite and carbon black were used as conductive additives. The mixture of PVDF and carbon black (PVDF/C) was simulated as a coating around the active material and graphite particles, as in prior work [18]. Open spaces were presumed to be filled with electrolyte, i.e. $LiPF_6$ in ethylene carbonate–diethyl carbonate (EC/DEC 1:1, v/v). Cathode compression experiments were used to validate the conduction modeling; validated conductivities were then used in battery performance simulations.

2.1. Experiments

2.1.1. Materials and compression of cathode system

Cathode electrode was constructed by combining 81.6 wt% $Li(Ni_{1/3}Co_{1/3}Mn_{1/3})O_2$ (Seimi Chemical), 4 wt% SFG-6 graphite (Timcal), 6.4 wt% acetylene black (Denkon), and 8 wt% PVDF binder (Kureha); fabrication was accomplished in several steps, including a compression and drying sequence. They were fabricated at Lawrence Berkeley National Laboratory by Drs. Battaglia and Gao. Table 3 shows cathode thicknesses and the volume fractions of each constituent phase during compression. To construct the cathode, a conductive glue was first made via mixture of acetylene black and PVDF, with a weight ratio of 4:5. The mixture was agitated for 30 min at 70% power using a Branson 450 Sonicator, to improve carbon black dispersion. The conductive glue was blended with $Li(Ni_{1/3}Co_{1/3}Mn_{1/3})O_2$ and graphite using Polytron PT10-3S Homogenizer at 3000–5000 rpm for 5 min. The slurry was poured

Table 2
Material properties of cathode system, electrolyte, and anode.

Parameter	Cathode system			Electrolyte	Anode
	$Li(Ni_{1/3}Co_{1/3}Mn_{1/}3)O_2$[a]	Graphite[a]	PVDF/C[a]	$LiPF_6$ (1 M) in EC/DEC (1:1)[a]	Li[a]
Particle size (μm)	11.04	7.45	–	–	–
Mass density ($g\,cm^{-3}$)	4.75	1.95	1.86	1.23	0.53
Bulk conductivity ($S\,m^{-1}$)	1.06×10^{-3}	1.67×10^{4}	760	0.52	1.20×10^{7}
Diffusion coefficient ($m^2\,s^{-1}$)	–	–	–	1.2×10^{-9}	–
Reference	[18]	[34]	[18]	[35,36]	[34]

[a] Material.

Table 3
Cathode thickness and volume fraction of active material, graphite, PVDF, and carbon black during compression at different porosities.

Porosity (%)	Active material (%)	Graphite (%)	Carbon black (%)	PVDF (%)	Thickness (μm)
50	31.8	3.8	6.1	8.3	200.0
40	38.2	4.6	7.3	10.0	166.7
30	44.5	5.3	8.5	11.6	142.9

against a Mitutoyo doctor blade holder, and spread evenly across the blade. The blade was set at a height of 250 μm for casting. Trace NMP solvent was spread on the perforated glass table top of the casting machine; then an Al foil was overlaid on the material, to serve as a current collector. The Al foil was then held to the glass by vacuum and the trace NMP. The ratio of the height of the blade and the final electrode thickness was set to approximately 3:1 of the final target thickness. The laminate was then dried at 120 °C for 12 h under high vacuum. The cathode was then compressed by rolling and cathode electrodes with assigned porosity were obtained by controlling final cathode thickness.

2.1.2. Measurement of electronic conductivity

The conductivity of the prepared cathode electrode was measured using an inline four-point-probe technique [37]. The same procedure indicated in Ref. [37] was adopted here. In summary, the constant current source was provided from the outer two probes by a Maccor battery test system Series 4000; the voltage difference was measured from the inner two probes by an HP 34401A multimeter, and two different probe spacing distances were used. In each sample, five random points were picked for conductivity measurement.

2.1.3. Microstructure of cathode system

FEI Quanta 3D scanning electron microscopy (SEM) was used to observe the microstructure of the cathode system. SEM pictures were taken in two different directions of view angles as Fig. 1 shows. Specimens for side view were frozen in liquid nitrogen and a razor blade was then used to provide a clean cut surface for which to examine the internal microstructure of the material, with minimal shearing.

2.2. Simulations

2.2.1. Packing architecture and conduction modeling

The simulations were performed as described in Ref. [18]. The simulations were used to estimate effective conductivity, effective ionic conductivity, and effective diffusion coefficient. Briefly, the architecture of the composite cathode, comprised of active material, graphite, carbon black, and PVDF, was generated via elastic collision modeling. Periodic boundary conditions were assigned to *x*-, *y*-, and *z*-directions to achieve computational efficiency. The radius of active materials was set to 0.15 of the representative volume; the semi-axes of graphite were dependent upon the size of active materials. The graphite was assumed as a disk-like ellipsoid with aspect ratios *a*/*b*, *a*/*c* and *b*/*c* (*a*, *b*, and *c* are the length of three semi-axes) set to 1, 7.4 and 7.4, respectively. Finite element meshing was performed using a voxelation method, to prevent mesh-induced singularities. Voxels of $100 \times 100 \times 100$ were assigned to the representative volume. A cubic element with each side of 1 unit length enclosing the voxel was generated, with an assigned material property. ABAQUS/STANDARD [38] was used for steady state conduction and diffusion analysis. Effective properties of conduction and diffusion of the representative volume were then calculated by applying potential difference in the *z*-direction. Porous regions were assumed to be fully occupied by the electrolyte phase. Simulation results of solid phase were later compared with experimental results to validate the conductivity simulations. Five simulation realizations were generated for each permutation of conditions studied.

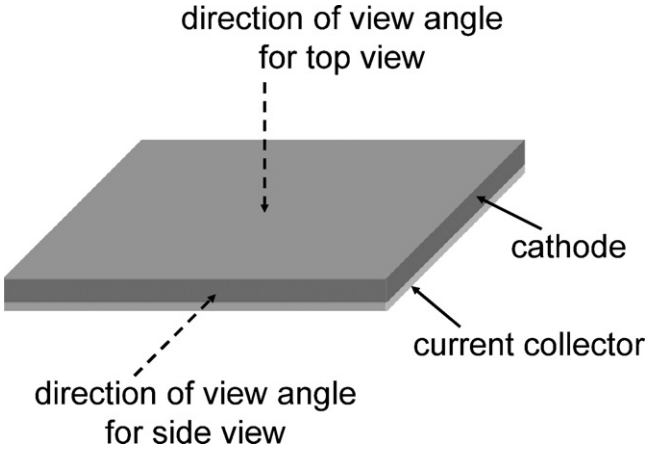

Fig. 1. Schematic illustration of direction of view angle for SEM.

Two types of simulations were performed. In the first type, uniform structures were assumed. In the second type, cathodes were assumed to be comprised of multiple layers, with conductivities in each layer based upon their density. This second group of simulations was performed based on the interrogation of materials structure, and the non-uniformity in packing, in real materials, as shown via scanning electron microscopy (SEM).

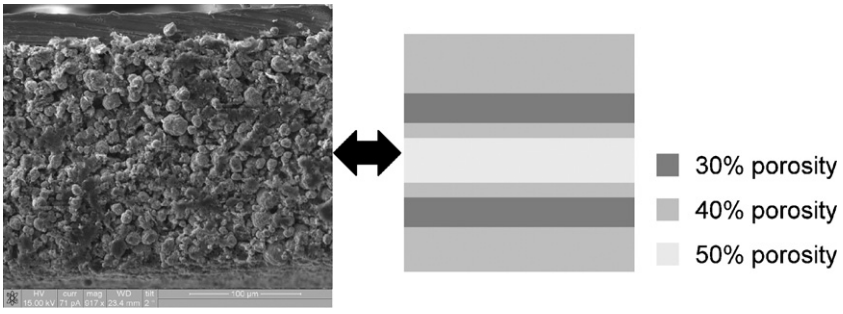

Fig. 2. SEM picture and schematic figure of multi-layer cathode electrode with 40% porosity.

Table 4
Governing equations of each simulated domain: 1D porous electrodes and 2D spherical particle.

Description	Region				
	1D domain			2D domain	
	Anode	Separator	Cathode		Cathode spherical particle
Electrical conduction in solid phase	$\nabla(-\kappa_{1,\text{neg}}\nabla\phi_1) = 0$ (1)	–	$\nabla(-\kappa_{1,\text{eff}}\nabla\phi_1) = S_a j_{\text{loc}}$ (2)		–
Current balance in electrolyte phase	–	$\nabla\left\{-\kappa_{2,\text{eff}}\nabla\phi_2 + \frac{2RT\kappa_{2,\text{eff}}}{F}\left[1+\frac{\partial}{\partial c_2}\ln f\right]\times[1-t_+]\nabla(\ln c_2)\right\} = 0$ (3)	$\nabla\left\{-\kappa_{2,\text{eff}}\nabla\phi_2 + \frac{2RT\kappa_{2,\text{eff}}}{F}\left[1+\frac{\partial}{\partial c_2}\ln f\right]\times[1-t_+]\nabla(\ln c_2)\right\} = S_a j_{\text{loc}}$ (4)		–
Mass balance in electrolyte phase	–	$\varepsilon\frac{dc_2}{dt} + \nabla(-D_{2,\text{eff}}\nabla c_2) = 0$ (5)	$\varepsilon\frac{dc_2}{dt} + \nabla(-D_{2,\text{eff}}\nabla c_2) = \frac{S_a j_{\text{loc}}(1-t_+)}{F}$ (6)		–
Ionic diffusion in solid phase	–	–	–		$r^2\frac{dc_1}{dt} + \nabla(-r^2 D_1\nabla c_1) = 0$ (7)

In Fig. 2, the left-hand side is the SEM picture from experiment with total porosity of 40% controlled by compression. The right-hand side is the schematic illustration of layer structure with different local porosity distributions. Though the total porosity was 40%, local porosity varied, in all likelihood due to nonaffine deformation induced by electrode compression. The schematic on the left illustrates that a cathode with an overall porosity of 40% can be modeled as a multi-layered electrode with porosities of 30%, 40% and 50%; the fractions of each porosity can be determined based on the image analysis of several SEM images. A cathode of 50% porosity was modeled as manufactured; at this porosity, the cathode was uncompressed. Hence, a multi-layer model for this cathode was not needed, or implemented.

2.2.2. Battery performance modeling

A model Li|Li($Ni_{1/3}Co_{1/3}Mn_{1/3}$)O_2 system with electrolyte EC/DEC (1:1, v/v) and $LiPF_6$ salt was used to evaluate battery performance for various cathode designs. Li metal was selected as anode electrode to eliminate limited reaction rate in anode. The theoretical capacity of the lithium metal is much higher than the one for Li($Ni_{1/3}Co_{1/3}Mn_{1/3}$)O_2. In real applications, excess lithium is used to assure full utilization of the cathode, and to compensate for consumption of the active mass by side reactions in electrolyte. Side reactions were neglected in the current study. In the current work, the anode thickness was calculated based on the theoretical capacity provided by the cathode, and the capacity ratio of the anode-to-cathode is one. The separator was not modeled as a discrete layer, since the cathode alone was optimized. The electrolyte was assumed to have a thickness of 50 μm. The electrode area was 2.4×10^{-3} m^2.

Li-ion battery is significantly affected by discharge conditions such as current rate and cutoff voltage. In our objectives, we would like to identify optimal schema for high energy Li($Ni_{1/3}Co_{1/3}Mn_{1/3}$)O_2 cells for HEV application. Therefore, a 3*C* discharge rate was used to meet the plug-in HEV battery goals from United States Council for Automotive Research [39]. 3.0 V was selected as cutoff voltage, which is a common and reasonable value. However, our simulation and optimization technique is not limited to any specific operating condition. In our technique, different cathode designs as well as different operating conditions can be selected to meet different applications.

This model was modified from 1D porous electrode model coupled with 2D spherical particle diffusion modeling [21]. Effective material properties calculated from the previous section were introduced in this model. The model includes solid phase electrical conduction using current balance based on Ohm's law, ionic conduction in electrolyte phase, ionic diffusion in electrolyte phase in 1D domain, and ionic diffusion in cathode spherical particles in 2D domain. The governing equations of each region are summarized in Table 4, where subscript 1 denotes the solid phase, subscript 2 denotes the electrolyte phase, subscript eff denotes the effective material property, subscript neg denotes the material properties of negative electrode, κ is conductivity, ϕ is potential, S_a is the specific surface area, j_{loc} is the local current density, R is the gas constant, T is the temperature, F is Faraday's constant, f is the ionic activity factor, D is the diffusion coefficient, t_+ is the cationic transport number, c is the cationic concentration, and r is the radius of the particle. 0.4 is used for cationic transport number in the simulation. The diffusion coefficient used for the Li in $Li_x(Ni_{1/3}Co_{1/3}Mn_{1/3})O_2$ was an averaged value from the diffusion coefficient of $Li_x(Co_{0.5}(NiMn)_{0.25})O_2$ and $Li_x(Li_{0.08}Co_{0.16}(NiMn)_{0.38})O_2$ [40].

The initial conditions and the boundary conditions are shown in Tables 5 and 6, respectively, where *i*_app is the assigned current density. From Table 5, initial state of charge is 0.28. Bulter–Volmer

Table 5
Initial conditions of each simulated domain: 1D porous electrodes and 2D spherical particle.

Description	Region			
	1D domain			2D domain
	Anode	Separator	Cathode	Cathode spherical particle
Electrical conduction in solid phase	$\phi_1 = 0$ (1-1)	–	$\phi_1 = 4.4$ (2-1)	–
Current balance in electrolyte phase	–	$\phi_2 = 0$ (3-1)	$\phi_2 = 0$ (4-1)	–
Mass balance in electrolyte phase	–	$c_2 = 2000$ (5-1)	$c_2 = 2000$ (6-1)	–
Ionic diffusion in solid phase	–	–	–	$c_1 = 14,870$ (7-1)

Table 6
Boundary conditions of each simulated domain: 1D porous electrodes and 2D spherical particle.

Description	Boundary					
	Boundary node in 1D domain				Boundary line in 2D domain	
	1	2	3	4	Cathode surface	Other surface
Electrical conduction in solid phase	$\phi_1 = 0$ (8)	$-ng\nabla(-\kappa_{1,\text{eff}}\nabla\phi_1) = 0$ (9)	$-ng\nabla(-\kappa_{1,\text{eff}}\nabla\phi_1) = 0$ (10)	$-ng\nabla(-\kappa_{1,\text{eff}}\nabla\phi_1) = -i\_\text{app}$ (11)	–	–
Current balance in electrolyte phase	–	$-ng\nabla\left\{-\kappa_{2,\text{eff}}\nabla\phi_2 + \frac{2RT\kappa_{2,\text{eff}}}{F}\left[1 + \frac{\partial}{\partial c_2}\ln f\right] \times [1 - t_+]\nabla(\ln c_2)\right\} = i\_\text{app}$ (12)	–	$-ng\nabla\left\{-\kappa_{2,\text{eff}}\nabla\phi_2 + \frac{2RT\kappa_{2,\text{eff}}}{F}\left[1 + \frac{\partial}{\partial c_2}\ln f\right] \times [1 - t_+]\nabla(\ln c_2)\right\} = 0$ (13)	–	–
Mass balance in electrolyte phase	–	$-ng\nabla\{-D_{2,\text{eff}}\nabla c_2\} = \frac{i\_\text{app}}{F}$ (14)	–	$\nabla\{-D_{2,\text{eff}}\nabla c_2\} = 0$ (15)	–	–
Ionic diffusion in solid phase	–	–	–	–	$\nabla\{-D_1\nabla c_1\} = \frac{j_{\text{loc}}}{F}$ (16)	$\nabla\{-D_1\nabla c_1\} = 0$ (17)

Table 7
Upper bound and lower bound of each variable.

Variables	Bound	
	Lower bound	Upper bound
Active material (vf.%)	30	45
Graphite (vf.%)	0	7.5
PVDF/C (vf.%)	10	30
Cathode thickness (μm)	50	400

electrode kinetics were applied at the interfaces of electrode and electrolyte:

$$j_{\text{loc}} = i_0 \left\{ \exp\left(\frac{\eta F}{RT}\right) - \exp\left(\frac{-\eta F}{RT}\right) \right\} \tag{18}$$

with

$$\eta = \phi_1 - \phi_2 - E_{\text{ref}}(c_{1,\text{surf}}) \tag{19}$$

and

$$i_0 = k_0 \sqrt{c_2(c_{1,\max} - c_{1,\text{surf}})c_{1,\text{surf}}} \tag{20}$$

where i_0 is the exchange current density, E_{ref} is the open-circuit potential of the electrode particle, which is a function of c_1 at the surface ($c_{1,\text{surf}}$), k_0 is the reaction-rate constant, and $c_{1,\max}$ is the maximum surface concentration. The function of E_{ref} is estimated from discharge-capability plot at 0.09*C* [41].

In the battery performance simulation, four design variables with common design of upper and lower bounds were selected as shown in Table 7.

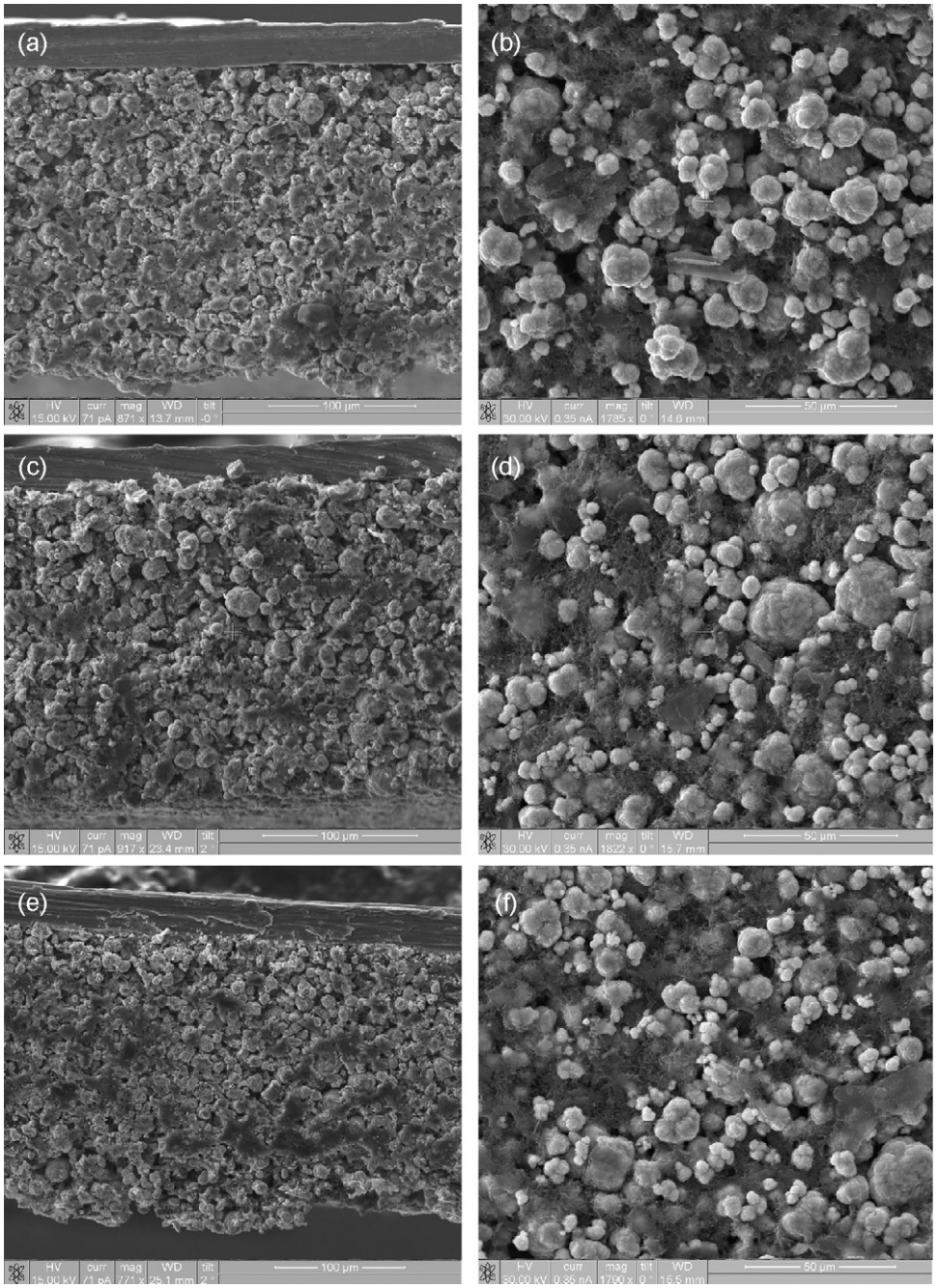

Fig. 3. SEM pictures of cathode electrodes at (a) 50% porosity side view, (b) 50% porosity top view, (c) 40% porosity side view, (d) 40% porosity top view, (e) 30% porosity side view and (f) 30% porosity top view.

2.3. Optimization of conductivities and battery performance

An optimization approach was introduced to design the cathode system. The cathode thickness was excluded in the variables for conduction modeling because the conduction model only simulates the unit cell of the cathode system, which is independent of cathode thickness. Numerical simulations (conduction modeling and battery performance modeling) were conducted at selected points. Electronic and ionic conductivities of cathode electrode, specific energy, and utilization of simulated battery were included in the objective functions.

3. Results

Fig. 3 includes the experimental results of SEM pictures of cathode electrode in side view and top view, with different porosities controlled by compression, where the active material comprises lighter particles surrounded by the darker PVDF/C phase. A decrease in porosity can be observed from the side views in Figs. 3(a), (c) and (e), corresponding to porosities of 50%, 40%, and 30%, respectively. These SEM pictures also show clearly that these are inhomogeneous structures. Further, the distribution of PVDF/C and cathode particles is less uniform with decreased porosity. Finally, as porosity decreases, active particles are apparently pushed into the PVDF matrix. The presence of distinct, active material particles, rather than active particles embedded in PVDF, becomes less pronounced at low porosity (per Fig. 3(b), (d), and (f)).

Experimental electrical cathode conductivities were 77 ± 41, 71 ± 25 and $105 \pm 63\,S\,m^{-1}$ for 50%, 40%, and 30% porosities, respectively (Fig. 4). Simulation results based on the single-layer assumption were 59 ± 5, 90 ± 1.4 and $150 \pm 9\,S\,m^{-1}$ for 50%, 40%, and 30% porosities, respectively. Simulation results based on the multi-layered assumption resulted in predicted cathode electrical conductivities of 70 ± 30 and $120 \pm 65\,S\,m^{-1}$ for 40% and 30% porosities, respectively.

Fig. 5 illustrates the composition of the simulated structure of the complementary solid phase and electrolyte phase obtained via our voxelated finite element conduction model. The solid phase was composed of cathode active material, graphite, and PVDF/carbon black coating. The porous region was assumed to be filled with electrolyte. Figs. 6–9 show the simulated structure of active material, PVDF/carbon coating, graphite, and electrolyte phase, respectively, at varying porosities.

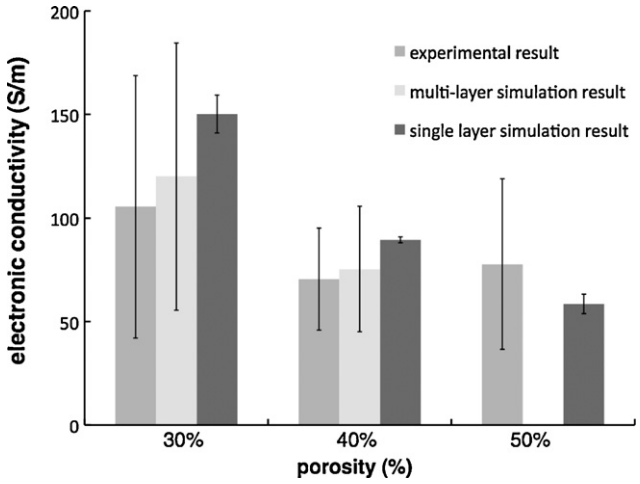

Fig. 4. Effective electronic conductivity of cathode electrode at different porosities from compression experiments and simulations.

Fig. 10 gives the simulation results for electronic and ionic conductivities, based on a single-layer cathode assumption at different porosities. These results demonstrate the trade-off of electronic and ionic conductivities for various cathode porosities. The value of electronic conductivity was increased by 2.5-fold, from 59 to $150\,S\,m^{-1}$ for 50% to 30% porosities; however, the ionic conductivity dropped from $0.18\,S\,m^{-1}$ with 50% porosity to $0.07\,S\,m^{-1}$ with 30% porosity.

Fig. 11 shows specific energy as a function of concentration saturation within particles at different cathode thicknesses. The difference between concentration saturation within particles and initial concentration ($2000\,mol\,m^{-3}$ in Table 5, which is equivalent to state of charge 0.28) represents the utilization. Compositions represented by each point were taken from multiple selections within ranges shown in Table 7. For cathode thicknesses larger than 100 μm, specific energy increased from 10 to $320\,Wh\,kg^{-1}$; utilization increased from 0.02 to 0.62. For cathode thicknesses ranging from 50 to 100 μm, specific energy and utilization were also positively related, but the results comprise another group, of lower specific energy and higher utilization. Utilization increased from

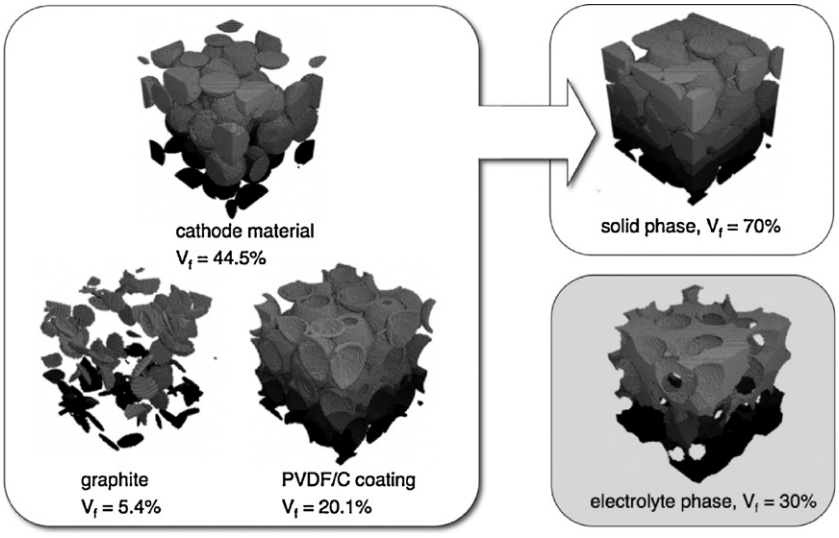

Fig. 5. Illustration of composition of cathode electrode: complementary solid phase and electrolyte phase.

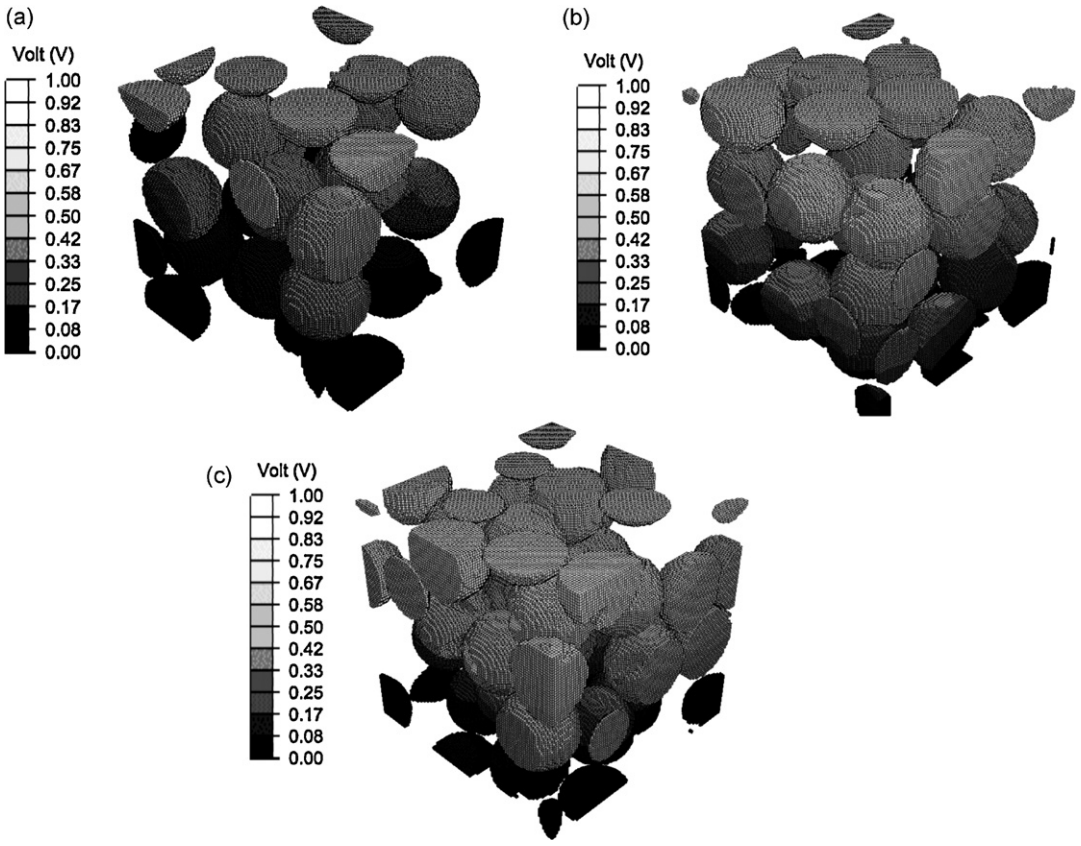

Fig. 6. Simulated random structure of cathode material particles at different porosities: (a) 50%, (b) 40% and (c) 30%.

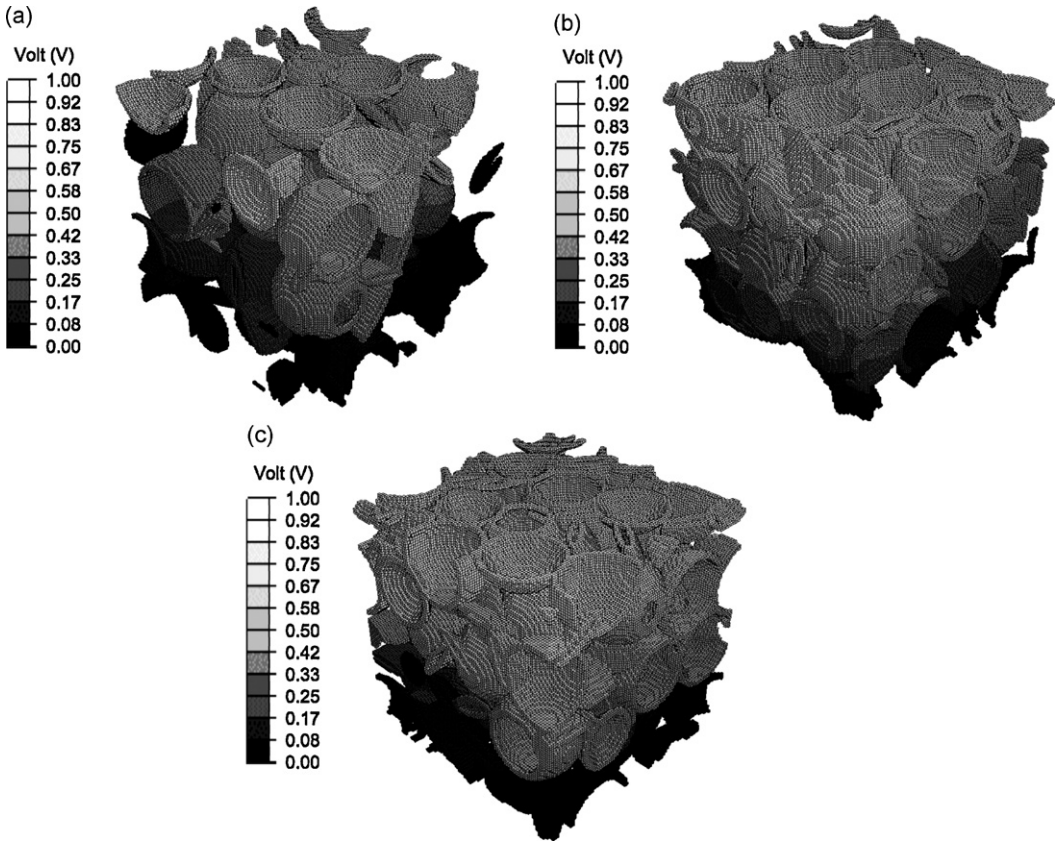

Fig. 7. Simulated random structure of PVDF/C at different porosities: (a) 50%, (b) 40% and (c) 30%.

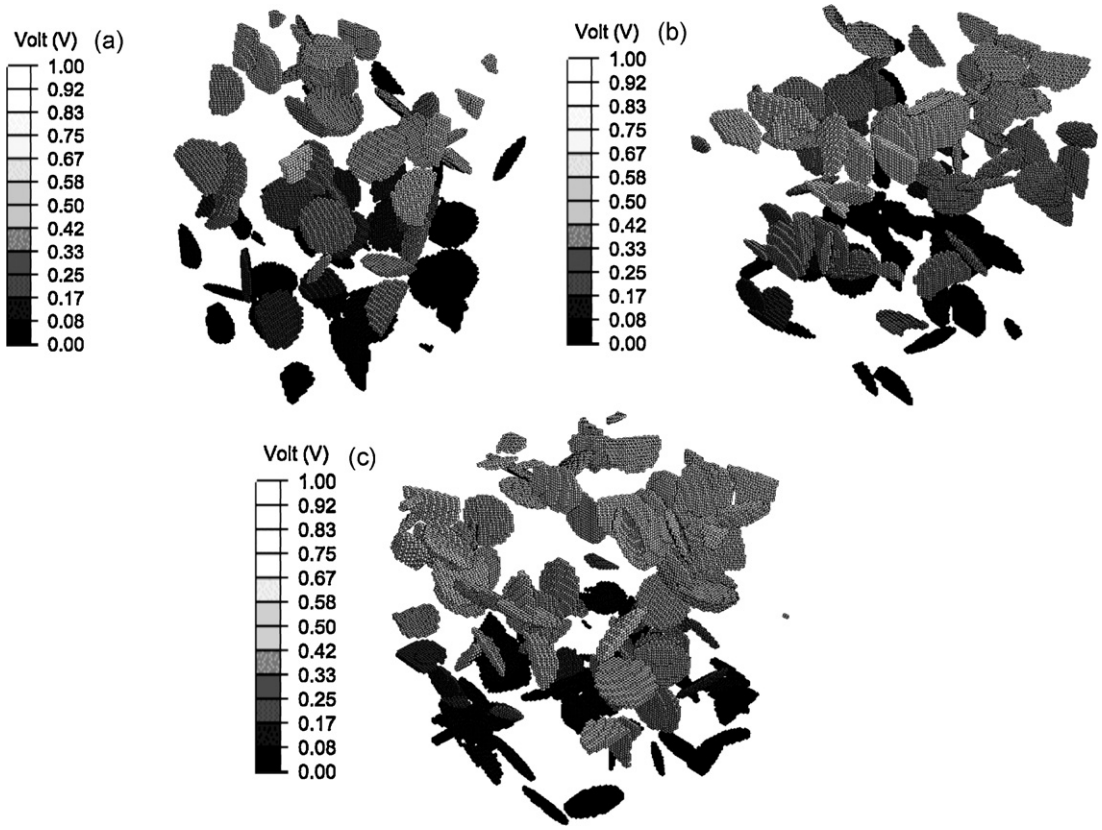

Fig. 8. Simulated random structure of graphite at different porosities: (a) 50%, (b) 40% and (c) 30%.

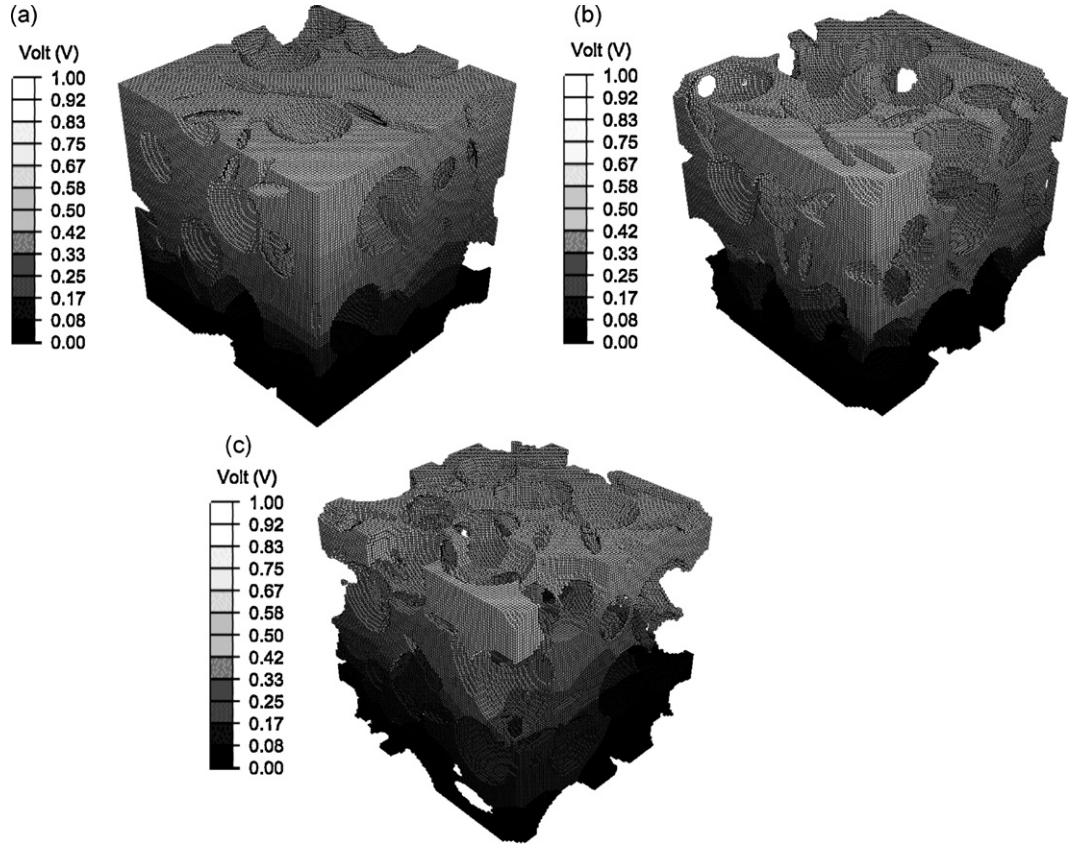

Fig. 9. Simulated random structure of electrolyte at different porosities: (a) 50%, (b) 40% and (c) 30%.

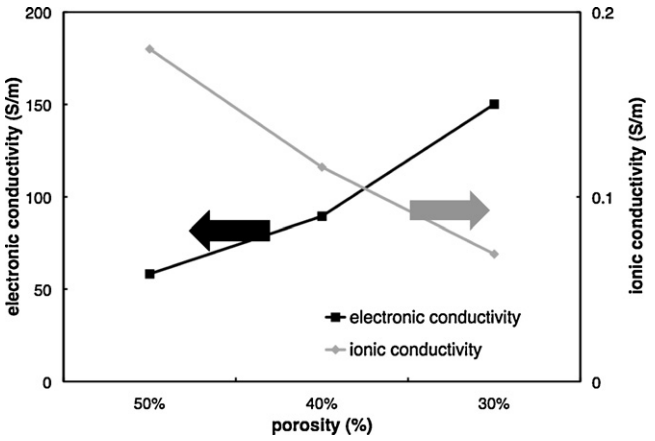

Fig. 10. Simulation results of electronic and ionic conductivities of single-layer cathode electrode at different porosities.

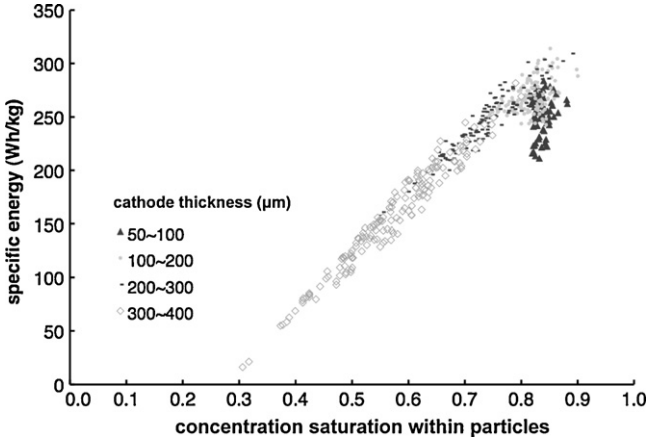

Fig. 11. Optimization results of specific energy as a function of utilization at different cathode thicknesses.

0.55 to a maximum of 0.62 with an increase in cathode thickness from 50 to 134 μm. Utilization decreased to 0.03 with a decrease in thickness to 400 μm. Fig. 12 illustrates some cases of discharge voltage versus utilization.

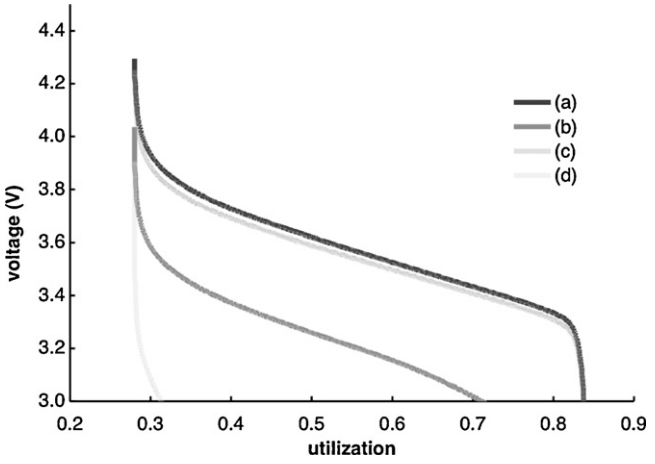

Fig. 12. Discharge curve generated from battery performance simulation of cathode electrode with 0% graphite, 10% PVDF/C and (a) 30% active material and 50 μm thickness, (b) 30% active material and 400 μm thickness, (c) 45% active material and 50 μm thickness, and (d) 45% active material and 400 μm thickness.

4. Discussion

As SEM pictures show in Fig. 3, the cathode system is not a perfectly homogeneous structure. Electrode compression, a common practice in production of cells, results in some degree of unavoidable, nonaffine deformation. Specifically, compressed cathodes, as do many compressed porous structures, show continuously varying porosity, rather than uniform, lower porosity, after undergoing deformation. Though direct modeling of this continuous grading is one means of studying this effect, in this case, discretized porosities in the thickness direction were used in order to simplify and reduce the cost of simulations. The gradation in porosity results in different (lower) overall conductivities than would occur with a more uniform, porous structure.

Theoretically, electronic conductivity should increase with increasing volume fraction of cathode for both single-layer and multi-layer simulation results, though there is a large discrepancy in standard deviations between these two models. Both single-layer and multi-layer simulation results show an increasing trend in conductivity with a decrease in porosity. Increase in solid phase connectivity by compression enhances electronic conductivity. However, multi-layer simulation results showed wider deviations, compared with single-layer simulation results. Simulated single-layer structures based on well-randomized collision realizations, with perfectly coated particles, produced smaller deviations in predicted conductivities. On the other hand, multi-layer cathodes showed a much wider range of deviation in conductivities due to non-uniform layered structure, which varied the amount of percolated paths for electrons and resulted in larger differences in conductivities.

Single-layer simulation results provided predictions of homogeneous cathode structure for an essentially ideal manufacturing process. Thus, these results may be thought of as the best-achievable in a real process, possibly attainable by reducing strain rate in compression. One needs to be cautious in manufacturing technique in order to prevent non-uniformity, which leads to unexpected results such as in the case of 40% porosity.

There is a trade-off between ionic and electronic conductivity; neither best ionic nor best electronic conductivity ensures the highest specific energy. Simulated structural results demonstrate the complementarity of solid and liquid phases. With reductions in porosity, more active material or conductive additives can be added in the solid phase, which results in higher electronic conductivity. However, cathodes with less porosity have intrinsically slower ion transport, which limits the reaction and lowers specific energy.

It is sufficient to use highly conductive surface coatings only, versus using both larger graphite particle and coating, to obtain high specific energy. In the studied variable ranges, cathode systems with 36.2% active material, 0% graphite, 10% PVDF/C and 192.5 μm thickness result in the highest specific energy of 323.5 Wh kg^{-1}. As our previous study shows [18], the PVDF/C coating phase creates a percolation base on active material spherical particulate system, which boosts its effective conductivity. It is possible to use graphite to further increase conductivity, but this will not contribute to higher specific energy.

Clearly, optimal design is needed to determine cathode thickness and volume fraction of active material. Ion transport, cathode capacity, and mass balance effect of active material are important factors on utilization. For thicker cathode electrode (250–400 μm), long ion transporting distance limits reaction rate, resulting in lower utilization. In order to improve utilization in thicker electrode, selection of low volume fraction active material to obtain more porosity is a better strategy. On the other hand, cathode capacity and mass balance effect of active material explain lower utilization in thinner electrode (50–100 μm). Fig. 13 shows the upper bound and lower bound of weight ratio of active material to

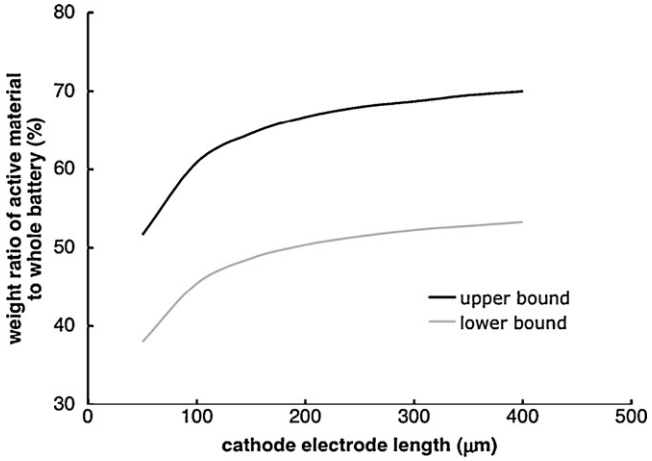

Fig. 13. Upper bound and lower bound of weight ratio of active material to whole battery in studied cases.

whole battery, where the weight ratio decreases with decrease in cathode electrode thickness. Therefore, even though ion has shorter transporting distance in thinner cathode, relatively lower capacity due to mass balance effect of active material also results in lower utilization. In thinner electrodes, more active material is required, rather than porosity, to improve specific energy since liquid limitation is not the dominant issue.

5. Conclusions and future work

A method was presented to investigate relationships between ionic and electronic conductivity in the Li-ion battery cathode system, and correlate the conductivity to specific energy for best cathode design. Cathode electrode was optimized for best specific conductivity at 3*C* rate and the highest specific energy of 323.5 Wh kg^{-1} was obtained by selection of 36.2% active material, 0% graphite, 10% PVDF/C, and 192.5 μm cathode thickness.

One key finding is that there is a trade-off between ionic and electronic conductivity, and neither best electronic nor ionic conductivity can achieve best specific energy. Monotonically increasing electronic conductivity by adding more conductive additive particles is not necessary since highly conductive surface coatings provide sufficient percolated path. Also, compressing the cathode system in order to obtain higher electronic conductivity and theoretical capacity density does not seem desirable in terms of specific energy for the ranges of materials studied.

Generally, design of cathode electrode for higher specific energy also creates higher utilization and specific power. To improve performance, it is important to consider the effect of cathode thickness and volume fraction of active material with regard to the ion transportation, cathode capacity, and mass balance effect of active material. Even though specific energy was set as the only objective function for current research, high utilization of 0.6 and high specific power of 1614 W kg^{-1} could be achieved.

We demonstrated the importance of cathode design and provided a baseline to optimize cathode composition with additives to obtain the best specific energy. We also compared the simulated result of electronic conductivity with experimental results. This comparison can be the baseline of our ionic conductivity prediction. A good battery design also relies on the optimization of electrolyte and anode in both geometry and material. Operation condition is another major factor for battery performance. In our next step, more design variables such as material and geometry of each cell component, and operating condition will be included as the future work, as well as battery performance comparison between simulation and experiment.

Acknowledgements

This work was generously supported by the Department of Energy BATT Program (Dr. Tien Duong, Program Director, DOE). Additional support was provided by the Ford Motor Company (Mr. Ted Miller and Mr. Kent Snyder, Program Directors) and Army Research Office (Dr. Bruce LaMattina, Program Director). We also thank Dr. Wei Shyy (University of Michigan) for his advisement on the use of optimization approaches, and Dr. Vincent S. Battaglia, Dr. Gao Liu, and Dr. Honghe Zheng at LBNL for provision of samples and data which are compared with our numerical predictions. We gratefully acknowledge the above-mentioned sponsors and colleagues.

References

[1] K. Zaghib, J. Shim, A. Guerfi, P. Charest, K.A. Striebel, Electrochemical and Solid-State Letters 8 (2005) A207–210.
[2] S.-T. Myung, M.H. Cho, H.T. Hong, T.H. Kang, C.-S. Kim, Journal of Power Sources 146 (2005) 222–225.
[3] D.-C. Li, T. Muta, L.-Q. Zhang, M. Yoshio, H. Noguchi, Journal of Power Sources 132 (2004) 150–155.
[4] J. Newman, K.E. Thomas-Alyea, Electrochemical Systems, John Wiley & Sons, New Jersey, 2004, pp. 518–519.
[5] K.E. Thomas, S.E. Slop, J.B. Kerr, J. Newman, Journal of Power Sources 89 (2) (2000) 132–138.
[6] C. Wang, L. Taherabadi, G. Jia, S. Kassegne, J. Zoval, M. Madou, Proceedings of the SPIE—The International Society for Optical Engineering 5455 (1) (2004) 295–302.
[7] R.S. Rubino, H. Gan, E.S. Takeuchi, Journal of the Electrochemical Society 148 (9) (2001) A1029–A1033.
[8] S.P. Sheu, C.Y. Yao, J.M. Chen, Y.C. Chiou, Journal of Power Sources 68 (2) (1997) 533–535.
[9] R. Vacassy, H. Hofmann, N. Papageorgiou, M. Gratzel, Journal of Power Sources 81 (1999) 621–626.
[10] C.-H. Lu, S.-W. Lin, Journal of Power Sources 97–98 (2001) 458–460.
[11] T. Kawamura, M. Makidera, S. Okada, K. Koga, N. Miura, J.-I. Yamaki, Journal of Power Sources 146 (1–2) (2005) 27–32.
[12] U. Lafont, C. Locati, E.M. Kelder, Solid State Ionics, Diffusion & Reactions 177 (35–36) (2006) 3023–3029.
[13] V. Srinivasan, J. Newman, Journal of the Electrochemical Society 151 (10) (2004) A1530–A1538.
[14] S. Ahn, Y. Kim, K.J. Kim, T.H. Kim, H. Lee, M.H. Kim, Journal of Power Sources 82 (1999) 896–901.
[15] J.S. Sakamoto, B. Dunn, Journal of the Electrochemical Society 149 (1) (2002) A26–A30.
[16] K. Zaghib, J. Shim, A. Guerfi, P. Charest, K.A. Striebel, Electrochemical and Solid State Letters 8 (4) (2005) A207–A210.
[17] C.M. Julien, K. Zaghib, A. Mauger, M. Massot, A. Massot, A. Ait-Salah, M. Selmane, F. Gendron, Journal of Applied Physics 100 (6) (2006) 63511-1–63511-7.
[18] Y.-H. Chen, C.-W. Wang, G. Liu, X.-Y. Song, V.S. Battaglia, A.M. Sastry, Journal of the Electrochemical Society 154 (10) (2007) A978–A986.
[19] C.-W. Wang, A.M. Sastry, Journal of the Electrochemical Society 154 (11) (2007) A1035–A1047.
[20] J. Newman, W. Tiedemann, AIChE Journal 21 (1) (1975) 25–41.
[21] M. Doyle, J. Newman, A.S. Gozdz, C.N. Schmutz, J.-M. Tarascon, Journal of the Electrochemical Society 143 (6) (1996) 1890–1903.
[22] E. Deiss, D. Haringer, P. Novak, O. Haas, Electrochimica Acta 46 (26–27) (2001) 4185–4196.
[23] E. Barsoukov, D.H. Kim, H.S. Lee, H. Lee, M. Yakovleva, Y. Gao, J.F. Enge, Solid State Ionics 161 (1–2) (2003) 19–29.
[24] B.Y. Liaw, R.G. Jungst, G. Nagasubramanian, H.L. Case, D.H. Doughty, Journal of Power Sources 140 (1) (2005) 157–161.
[25] B.Y. Liaw, G. Nagasubramanian, R.G. Jungst, D.H. Doughty, Solid State Ionics 175 (1–4) (2004) 835–839.
[26] J.N. Reimers, Journal of Power Sources 54 (1) (1995) 16–19.
[27] J.W. Halley, Y. Duan, Journal of Power Sources 110 (2) (2002) 383–388.
[28] M.E. Garcia, E. Webb, S.H. Garofalini, Journal of the Electrochemical Society 145 (6) (1998) 2155–2164.
[29] S.H. Garofalini, P. Shadwell, Journal of Power Sources 89 (2) (2000) 190–200.
[30] Z Chen, J.R. Dahn, Electrochemical and Solid-State Letters 6 (11) (2003) A221–A224.
[31] G.T.-K. Fey, R.F. Shiu, T.P. Kumar, C.L. Chen, Materials Science & Engineering B 100 (3) (2003) 234–243.
[32] S. Mandal, J.M. Amarilla, J. Ibanez, J.M. Rojo, Journal of the Electrochemical Society 148 (2001) A24–A29.
[33] A.S. Skapin, M. Gaberseck, R. Dominko, M. Bele, J. Drofenik, J. Jamnik, Solid State Ionics 167 (2004) 229–235.
[34] http://www.matweb.com (04.20.08).
[35] S.-I. Lee, U.-H. Jung, Y.-S. Kim, M.-H. Kim, D.-J. Ahn, H.-S. Chun, Korean Journal of Chemical Engineering 19 (2002) 638–644.

[36] Y.F. Zhou, S. Xie, X.W. Ge, C.H. Chen, K. Amine, Journal of Applied Electrochemistry 34 (11) (2004) 1119–1125.
[37] C.-W. Wang, A.M. Sastry, K.A. Striebel, K. Zaghib, Journal of the Electrochemical Society 152 (5) (2005) A1001–A1010.
[38] ABAQUS/STANDARD, Hibbitt, Karlsson & Sorensen Inc.
[39] http://www.uscar.org/commands/files_download.php?files_id=156.
[40] K. Eberman, L. Krause, The 204th Electrochemical Society Meeting, Orlando, FL, 2003.
[41] N. Yabuuchi, T. Ohzuku, Journal of Power Sources 119–121 (2003) 171–174.